

## Tropopause folding at satellite-observed spatial gradients: 2. Development of an empirical model

A. J. Wimmers<sup>1</sup> and J. L. Moody

Department of Environmental Sciences, University of Virginia, Charlottesville, Virginia, USA

Received 10 September 2003; revised 24 June 2004; accepted 28 July 2004; published 6 October 2004.

[1] We develop an empirical model that estimates the horizontal distribution of tropopause folds based primarily on a robust relationship between upper tropospheric specific humidity gradients and tropopause folding. The specific humidity gradients are resolved by the altered water vapor (AWV) product, developed from the GOES imager water vapor channel. Unexpectedly, no proportional relationship was found between tropopause fold size and AWV gradient magnitude beyond the one-to-one occurrence of strong gradients at tropopause folds. This indicates that tropopause folds do not commonly reach a “steady state” mass of ozone inside the fold. Rather, the mass of air must be controlled at least as much by the age of the fold and dynamical dispersion mechanisms that are not linearly related to the strength of the corresponding tropopause depression. This has important implications for the interpretation of lidar imagery and in situ ozone data at tropopause folds. In lieu of this result, a uniform fold size is assigned at all locations of modeled folding on the basis of the average of the folds used in parameterization. The model estimates the distribution of actively developing and residual tropopause folds, which is a useful method of tracking the dispersal of all stratospherically enhanced air in the troposphere and is unique to this observation-based model of tropopause folding. *INDEX TERMS*: 3362 Meteorology and Atmospheric Dynamics: Stratosphere/troposphere interactions; 3360 Meteorology and Atmospheric Dynamics: Remote sensing; 0368 Atmospheric Composition and Structure: Troposphere—constituent transport and chemistry; *KEYWORDS*: tropopause folding, specific humidity, ozone, lidar, water vapor channel, gradients

**Citation:** Wimmers, A. J., and J. L. Moody (2004), Tropopause folding at satellite-observed spatial gradients: 2. Development of an empirical model, *J. Geophys. Res.*, 109, D19307, doi:10.1029/2003JD004146.

### 1. Introduction

[2] *Wimmers and Moody* [2004] optimized a strategy for locating tropopause folding signatures in satellite imagery. On the basis of these results, a synoptic-scale empirical model is developed here using only satellite derived product imagery. It predicts the presence of stratospheric air contained within tropopause folds in the troposphere. This model is built from a theoretical relationship between satellite-observed spatial gradients in GOES specific humidity and the physical mechanisms of tropopause folding.

[3] In the scientific literature, the types of models used to predict and estimate cross-tropopause transport are presently limited to either reanalyses or atmospheric models. In both these methods, the accuracy of mixing processes at the tropopause level is limited by the sparseness of initialization data, a low resolution of grid cells and a restriction of the reanalysis or model physics to predetermined “artificial

diffusion” mechanisms that may not adequately capture the true dispersion of atmospheric tracers at the appropriate scales, as discussed below.

[4] Previous studies that examine cross-tropopause transport through global reanalysis data sets are valuable, however these data do not provide a complete picture of the various attributes of cross-tropopause exchange. Not surprisingly, studies using global reanalyses emphasize the role of large-scale phenomena such as circulation associated with summer monsoons [*Chen*, 1995], Rossby wave breaking and midlatitude baroclinic activity [e.g., *Seo and Bowman*, 2001] on STE. Because the reanalyses remain rooted in a low-resolution operational observation network, they miss or de-emphasize mesoscale (or smaller) phenomena inherently. This occurs regardless of whether the mesoscale or smaller phenomena are dominant features in the real atmosphere. For example, the Measurement of Ozone by Airbus In-Service Aircraft (“MOZAIC”) program compiled thousands of ozone and water vapor soundings on European transcontinental commercial aircraft flights and discovered quasi-horizontal layers of high ozone and low water vapor in roughly 11% of the volume of the midlatitude troposphere [*Newell et al.*, 1999]. The chemical signature of these layers, which had an average vertical width of 0.86 km, strongly indicated a stratospheric origin. It is noteworthy that such

<sup>1</sup>Now at Cooperative Institute for Meteorological Satellite Studies, University of Wisconsin-Madison, Madison, Wisconsin, USA.

layers had never before been reported from any treatment of a reanalysis data set. This shows that small-scale differences between global reanalyses and the real state of the atmosphere cannot be ignored when examining transport near the tropopause, because even small-scale phenomena can have first-order effects on atmospheric composition.

[5] Recent intercomparison and validation of reanalysis-based methods of estimating STE reveals the various levels of success of each method in overcoming the intrinsic limitations of the underlying atmospheric analyses. *Stohl et al.* [2003] provides a thorough review of reanalysis-based methods of estimating STE.) The most popular methods are the “Wei formula” [Wei, 1987], trajectory modeling and Lagrangian particle dispersion. The Wei formula is a diagnostic applied to Eulerian models, which has been shown to create significant errors where the cancellation of large terms is involved [Wirth, 1995; Wirth and Egger, 1999; Gettelman and Sobel, 2000]. This requires significant spatial and temporal averaging to arrive at useful results. Trajectory models [Wirth and Egger, 1999; Kowol-Santen et al., 2000; Stohl, 2001; Meloan et al., 2001; Wernli and Bourqui, 2002; Seo and Bowman, 2002; Sprenger and Wernli, 2003] avoid this problem of cancellation error, but are lacking in convection and turbulence parameterizations in their advection calculations, which can lead to an underestimation of cross-tropopause flux that occurs by irreversible mixing [Meloan et al., 2003; Cristofanelli et al., 2003]. Trajectory models are further limited by the finite lifetimes of simulated parcels, which can fail to capture the recirculation of parcels back to their original source and lead to an overestimation of mixing in other locations. The Lagrangian particle dispersion method uses continuous trajectories and merges the grid-scale winds with individual particle stochastic fluctuations to account for turbulent eddies and subgrid convection [Stohl et al., 1998; Stohl and Thomson, 1999]. However, the parameterization of turbulence is still prone to large uncertainties in magnitude, location and time of occurrence [James et al., 2003]. In addition, each of these methods are naturally limited by the accuracy of their underlying reanalysis fields. In spite of the tremendous power of these methods of STE estimation, such intrinsic limitations can lead to conflicts between model results and phenomena that are readily apparent from observations, such as the failure to account for the mere presence of some tropopause folds [Vaughan et al., 2001].

[6] Furthermore, the use of current atmospheric models (in contrast to reanalyses) to adequately depict tropopause folding and the associated cross-tropopause flux at any resolution is by no means resolved. On the one hand, mesoscale models (at 80-km horizontal spacing and finer) of midlatitude cyclones have quite successfully simulated mixing at tropopause levels [e.g., Lamarque and Hess, 1994]. *Ravetta et al.* [1999] show a convincing agreement between a ground-based lidar measurement of a tropopause fold and the results of a 40-km MM5 simulation of an intense midlatitude cyclone. *Olsen et al.* [2000] and *Goering et al.* [2001] likewise find good agreement between the 40-km Mesoscale Analysis and Prediction System atmospheric model and TOMS total ozone imagery from another intense midlatitude cyclone. However, while mesoscale models have traditionally focused on simulating cross-tropopause transport during strong cyclone development,

their accuracy at capturing the mechanisms of STE at weaker upper air fronts (i.e., at general air mass boundaries such as those investigated in the work of *Wimmers and Moody* [2004] and during streamer breakdown) have not been explored as thoroughly, notwithstanding the quasigeostrophic model simulation of streamer breakdown by *Wirth et al.* [1997]. Thus there is still a need to explore smaller-scale mixing events and compare their relative contribution to the atmospheric chemical composition at all scales. GOES satellite observations, with high spatial and temporal resolution over a large domain, can be an effective tool to address this need.

[7] The purpose for developing an empirical model of tropopause folding is to add a uniquely independent, satellite observation-based, fine-scale, synoptic depiction of tropopause folding to the current array of diagnostic tools. *Wimmers and Moody* [2004] have shown a strong predictive relationship between tropopause folds and spatial gradients in both AWV-derived upper tropospheric specific humidity and TOMS total ozone. This paper continues along this path to test for a possible relationship between AWV gradient magnitude and tropopause fold magnitude, and then to use the results to parameterize an empirical model of tropopause folding activity based only on satellite imagery. Only AWV imagery is used here, because of its greater accuracy with the technique explored in the work of *Wimmers and Moody* [2004] and because of the advantages of geostationary imagery for observing evolving synoptic systems over a large domain.

[8] What follows in this paper is a reintroduction of the data (section 2), a discussion of the assumptions behind the relationship between AWV gradient magnitude and tropopause fold magnitude (section 3), an explanation of the methods used to test these assumptions (section 4), a presentation of the test results (section 5), the development of an empirical model of tropopause folding based on these results (section 6), a discussion of the model (section 7) and the summary and conclusions of this study (section 8). Appendix A contains the conversions and approximations used to put the data into usable form.

## 2. Data

[9] As in the work of *Wimmers and Moody* [2004], this study relates AWV imagery to airborne lidar observations of tropopause folds from the Tropospheric Ozone Production about the Spring Equinox (TOPSE) campaign from February to May of 2000. AWV imagery is a modification of the GOES “water vapor channel” using ancillary temperature fields to depict specific humidity in a vertically weighted average between 250 and 500 hPa [Wimmers and Moody, 2001]. Just as the displayed quantity of the water vapor channel is brightness temperature, the displayed quantity of the AWV derived product is “altered brightness temperature” (ABT) which varies with the log of the weighted specific humidity. By convention, the acronym “ABT” is used only when referring directly to the values within the AWV imagery. Otherwise, the acronym “AWV” is used in order to keep the nomenclature as consistent as possible. Throughout this paper, the term “AWV gradients” is used to refer to ABT gradients in the AWV imagery. Detailed specifications of the AWV imagery as well as the airborne

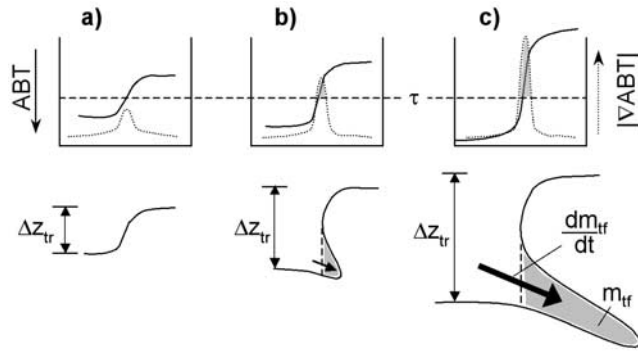


**Figure 1.** ABT and  $|\vec{\nabla}ABT|$  transects (top row) and corresponding tropopause geometries (bottom row) for three hypothetical scenarios. (a) Small increase in tropopause height ( $\Delta z_{tr}$ ) with no fold; (b) moderate increase in tropopause height corresponding to a small fold; (c) large increase in tropopause height corresponding to a large fold. The label “ $m_{tf}$ ” is mass per unit length of air in the tropopause fold, and  $dm_{tf}/dt$  is mass flux per unit length into the tropopause fold from the stratosphere.

ozone lidar are presented in the companion paper by *Wimmers and Moody* [2004].

### 3. Assumptions

#### 3.1. Initial Assumptions

[10] *Wimmers and Moody* [2004] established a one-to-one relationship between significantly high AWV gradient magnitudes and the occurrence of tropopause folds, with no apparent signs of spatial or temporal bias. Furthermore, the relationship created no false positives, meaning that every prediction of a tropopause fold was confirmed in an ozone lidar transect. However, this accomplishment by itself does not directly address what is arguably the most important aspect of tropopause folding, which is the associated mass flux between the stratosphere and the troposphere. Namely, does an AWV gradient that exceeds the threshold determined in the companion paper by *Wimmers and Moody* [2004] vary linearly with the size of its associated tropopause fold?

[11] Lidar cross sections provide an entry point for studying mass flux by revealing the size and shape of the layer of stratospheric air intruding into the troposphere, indicated by enhanced ozone concentrations. These qualities of the intrusion can then be directly related to their associated AWV gradient magnitudes to explore a possible relationship between lidar-measured and remotely sensed quantities. The simplest starting point for investigating this relationship is to assume a first-order linear proportionality:

$$\max\left(|\vec{\nabla}ABT| - \tau, 0\right) \propto \frac{dm_{tf}}{dt}, \quad (1)$$

where  $m_{tf}$  is the mass of the stratospheric air intruded into the troposphere in a tropopause fold per unit length,  $|\vec{\nabla}ABT|$  is the magnitude of the ABT gradient and  $\tau$  is the threshold magnitude that differentiates smaller, inconsequential variations in ABT from larger gradients associated with tropopause folding. The dimensions of the right-hand side are mass per unit length per unit time, which corresponds to flux in a vertical cross section such as in a lidar profile.

Figure 1 illustrates these terms. The term “per unit length” follows the convention used throughout this paper that “length” follows the direction of the tropopause fold oriented “lengthwise” along the tropopause break, and “width” describes the transverse direction, which is normally assigned to the  $x$  axis in tropopause fold cross sections.

#### 3.2. Remotely Sensed Gradient

[12] For simplicity, equation (1) assumes a zero-order discontinuity in the spatial gradients. In other words, the physical phenomena are assumed to correspond to a gradient magnitude at only one point in the horizontal distribution of  $|\vec{\nabla}ABT|$ . However, under real conditions, the boundary between differing air masses is better approximated as a first- or second-order discontinuity. This changes the focus of the approximations from a point value to an integration of values across a transect perpendicular to the boundary (written as “ $\perp$  transect” in the following equation). This quantity is referred to afterward as the remotely sensed gradient (RSG), and is compared directly to tropopause fold mass to test for a proportional relationship:

$$RSG \equiv \int_{\perp \text{ transect}} \max\left(|\vec{\nabla}ABT| - \tau, 0\right) ds. \quad (2)$$

#### 3.3. Practical Assumptions for the Study

[13] The circumstances of the TOPSE observations impose restrictions on this experiment that require additional assumptions. Lidar transects provide only a snapshot of the distribution of stratospheric tracers in the atmosphere and do not directly indicate flux. In this experiment, the mass of air in a tropopause fold must substitute for mass flux:

$$m_{tf} \propto \frac{dm_{tf}}{dt}. \quad (3)$$

The condition in which this equation becomes true is when the observed tropopause folds in the lidar images quickly reach steady state after their initiation. In a steady state, the influx of stratospheric air is balanced by physical dispersion beyond the recognizable boundaries of the fold. To be specific, the words “quickly reach steady state” mean that a measurement of the steady state condition is much more likely than a measurement of a development stage (or “growth stage”).

[14] However, the measurements in this study are of lidar ozone transects. Since ozone is measured directly from the lidar, it is important to compare the following two relationships as well:

$$m_{O_3} \stackrel{?}{\propto} m_{tf} \quad (4)$$

and

$$RSG \stackrel{?}{\propto} m_{O_3}, \quad (5)$$

where  $m_{O_3}$  is the mass of ozone per unit length of the fold.

[15] Finally, the experiment also tests for a relationship between the measured mass of a tropopause fold and its geometry:

$$W_{tf} \stackrel{?}{\propto} m_{tf}, \quad (6)$$

**Table 1.** Statistics of “Complete” Tropopause Fold Structures Resolved by TOPSE Ozone Lidar<sup>a</sup>

Flight	Fold	$W_{tf}$ , km	$m_{O_3}$ , kg m <sup>-1</sup>	$m_{tf}$ , kg m <sup>-1</sup> ·10 <sup>6</sup>	RSG, K
7	2	118	6.49	48.9	1.75
15	1	575	27.37	221	2.05
16	1	440	19.72	117	5.54
17	1	870	41.91	364	2.02
35	1	445	23.72	139	2.82
38	1	923	49.96	373	0.41
38	2	110	4.60	29.5	3.45
38	3	168	5.22	34.1	0.74
42	1	1299	125.08	850	3.50
		<i>261</i>	<i>33.78</i>	<i>242</i>	<i>2.48</i>
		<b>235</b>	<b>30.41</b>	<b>218</b>	N/A

<sup>a</sup>Terms defined in text. Mean values are shown in italics, while mean (N + 1) values are shown in boldface. N/A, not applicable.

where  $W_{tf}$  is the width of the tropopause fold. This relationship is important for developing a prediction of the location of tropopause folds from the satellite imagery and adds another hypothesis to be tested:

$$RSG \overset{?}{\propto} W_{tf}. \quad (7)$$

#### 4. Methods

[16] In the assumptions above, both  $m_{tf}$  (mass of a tropopause fold per unit length) and  $W_{tf}$  (transverse width of a tropopause fold) are assumed to be from cross sections orthogonal to the fold. Unfortunately, the lidar transects from TOPSE are neither orthogonal to the folds nor always sufficiently straight. Instead, methods must be applied to the data to extract terms that approximate the variables in this study. Most of this effort involves determining the angles of the cross sections and approximating continuous integrals, and is detailed in Appendix A.

[17] The main hypotheses of this study will be tested by confirming a relationship between the remotely sensed gradient and any of the following three quantities:  $m_{O_3}$ ,  $m_{tf}$  and  $W_{tf}$ . However, before that, the relationships between those three quantities are examined to confirm whether they can be treated as roughly proportional.

[18] Only a subset of the folds from *Wimmers and Moody* [2004] are examined here, because the fold must be measured over its entire width in order to retrieve its mass of air, mass of ozone and of course its width. This introduces a significant but unavoidable bias to the sampling of folds over TOPSE because wider folds were by their nature less likely to be sampled from end to end. Larger folds were missed in flight 05 because the lidar started in the middle of the fold, and in flight 36 because the fold reached outside the flight path. The effect of this bias will be discussed in turn.

#### 5. Relationships Between the Variables

[19] The results for the following discussion are presented in Table 1. First,  $m_{tf}$  and  $m_{O_3}$  have a strong, proportional relationship to each other as expected (Figure 2a). This primarily indicates that the area of the folds identified in this study had a similar average ozone mixing ratio. Had the ozone mixing ratio varied significantly between samples,

the regression would not have been as robust. Second,  $m_{tf}$  is proportional to the square of  $W_{tf}$  (Figure 2b). This makes sense because  $m_{tf}$  is integrated over a two-dimensional area, whereas  $W_{tf}$  is a one-dimensional distance. However, the square relationship depends heavily on the outlying point at the upper right of the curve (from flight 42), whose mass value is heavily influenced by a region that is actually a spatial interpolation of the lidar data. Thus the square relationship is not certain, and requires more data than is available to be thoroughly proved.

[20] Unexpectedly, Figure 3 shows that there is no relationship between remotely sensed gradients and any of the three quantities  $m_{O_3}$ ,  $m_{tf}$  or  $W_{tf}$ . Each of the three scatterplots also shows that the lack of a relationship in the regression is not even due to a small number of outliers that throw off a possible trend. In short, there is no confirmable relationship between the mass of air in a

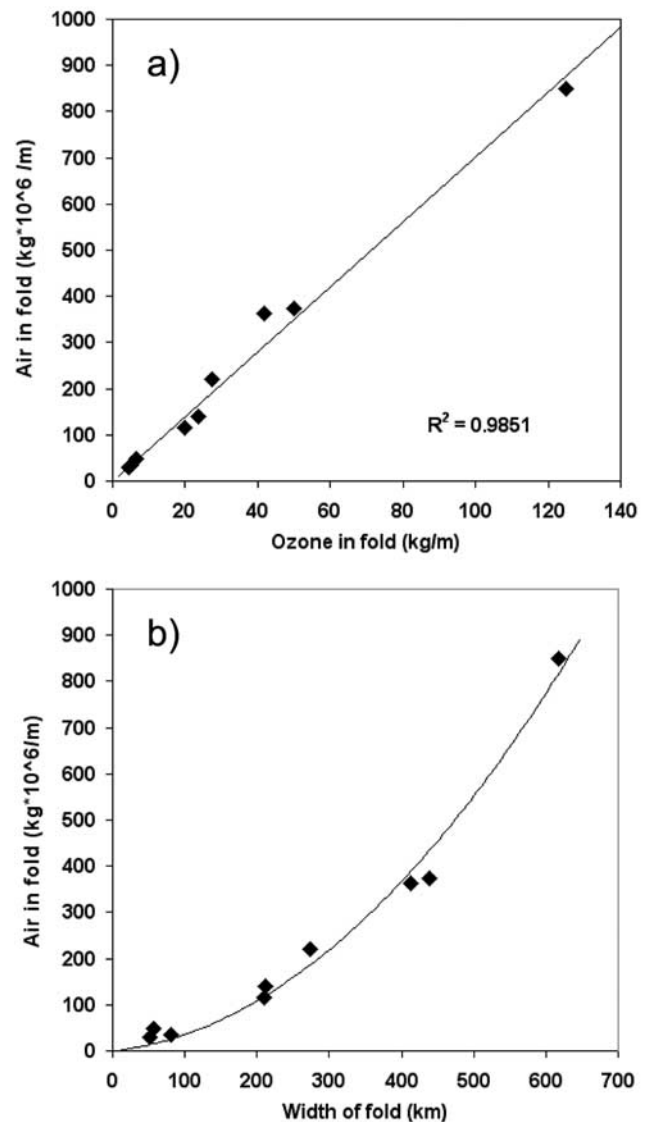
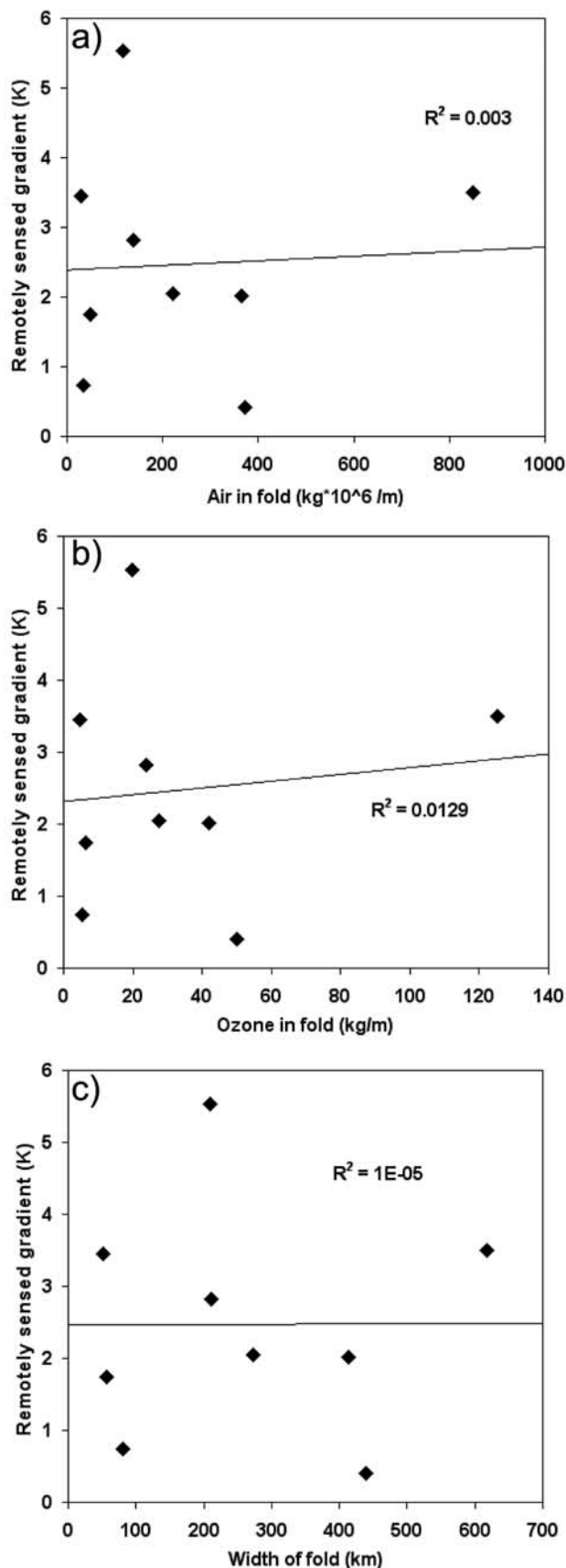


**Figure 2.** Mass per unit length of the air in the corresponding tropopause fold versus (a) mass per unit length of ozone in the corresponding tropopause fold and (b) width of the corresponding tropopause fold.



tropopause fold (as indicated by the distribution of high ozone mixing ratios) and the corresponding remotely sensed gradient, and there is no confirmable relationship between the width of a tropopause fold (as indicated by the distribution of high ozone mixing ratios) and the remotely sensed gradient.

[21] In spite of this mainly negative result there is one concrete observation about tropopause folding that is revealed by this study. If equation (1) is valid, then the results reveal that the “steady state” assumption of equation (3) is not valid. Rather, the mass flux of ozone from the stratosphere into the upper troposphere in the form of folding does not commonly reach an equilibrium with the flux out of the fold through dispersion. We can conclude that the mass of folded ozone measured in the lidar transects depends heavily on some combination of its age and mechanisms of dispersion that are not proportional to the size of the associated tropopause depression. These factors combined are probably much more important to the mass of ozone in the fold than the instantaneous influx of air from the stratosphere. This has important implications for the interpretation of any upper tropospheric lidar and in situ ozone data in the midlatitudes and subpolar domain.

[22] It must be noted that the data in Table 1 present a unique, normalized sample of tropopause fold widths and cross-sectional mass. This particular collection represents a four-month period around the spring equinox within a latitudinal domain between  $40^\circ$  and  $65^\circ\text{N}$  latitude. It is difficult to ascertain whether this is a “random” sample of measurements, because the number of measurements corresponding to particular types of synoptic feature such as dry air streamer boundaries, cyclogenesis, polar/subtropical boundaries and polar/arctic boundaries is very low. For the given samples, no trends were apparent between tropopause fold size and synoptic feature type or latitude. In addition, larger folds were less likely to be included in the collection, which offers one argument that the averages of folded mass and fold widths are in fact biased too low.

[23] The average values listed in Table 1 (average folded mass per unit length and average width of a tropopause fold) are of central importance to an empirical model that assigns a best estimate of folded mass and fold width to a ridge on any given gradient magnitude image. The most straightforward way of estimating folded mass and fold width would be to use the mean of these values. The mean of the values using  $N + 1$  samples is included in the table because fold 2 from flight 38 technically corresponded to two ridges [see *Wimmers and Moody, 2004*, section 4.3]. Thus this value is a more accurate prediction of the average folded mass and fold width per ridgeline. It is worth noting that the mean tropopause width (235 km) is in very good agreement with the typical range of observed crosswind tropopause fold widths (100–300 km) from the in situ aircraft observations of *Johnson and Viezee [1981]*. Finally, although the variance in these measurements suggests that

**Figure 3.** Remotely sensed gradient compared to (a) mass per unit length of the air in the corresponding tropopause fold, (b) mass per unit length of ozone in the corresponding tropopause fold, and (c) width of the corresponding tropopause fold.

applying the mean value would lead to significant errors in the model at any particular prediction, the cumulative effect of these errors over a large number of images would be reduced as long as the errors are spatially random. The use of this information in an empirical model will be explored in the following section.

## 6. Description of the Empirical Model

[24] Although AWV gradient magnitude is not a strong indicator of tropopause fold geometry, there is still a sufficient amount of information to build a predictive model of tropopause folding based on the AWV product. Its strengths and weaknesses will be explored as the model takes form. By its nature, the data used in this study is focused on the spatial distribution of tropopause folding and does not directly quantify the associated flux. Instead, the model focuses on identifying the presence of tropopause folds in the atmosphere, so it is named the tropopause fold presence (TFP) model.

[25] The overall approach of the TFP model is to place hypothesized tropopause folds at significant boundaries in the AWV imagery, extending into the troposphere in the appropriate directions. In this model, contours along the maximum slope of smoothed AWV gradients (“ridge lines”) define the modeled fold openings. The model assigns a tropopause fold extending at a constant width from this contour into the free troposphere toward the side with higher humidity, essentially forming the fold of dry air intruding beneath a layer of moist air. Figure 4 illustrates the process by which tropopause folds are determined from the AWV image. Model results can be calculated quickly: the normal computation time on a desktop PC using real-time imagery is two minutes after the acquisition of the satellite image. Further details can be found in the work of *Wimmers* [2003].

[26] The “coverage” of the folds is therefore the space bounded within these ribbons of modeled folds. On the basis of the parameterization from the previous section, the distance that describes the ribbon width is 2.11 great circle degrees (235 km). As stated previously, this value is a best estimate only. The result is a geographic distribution of area covered by modeled folds. Figure 4e demonstrates the location of modeled folds along the edges of the major upper tropospheric air mass boundaries. The nearly contiguous nature of the folds surrounding a trough of dry polar air in the mid-Pacific (A) is consistent with the observations of *Johnson and Vezee* [1981] that tropopause folds appeared along every upper air trough encountered by their campaign. The mid-Pacific trough is typical of the early stages of a large equatorward excursion of polar air during trough formation seen in the AWV imagery during winter and spring seasons. The other large and more mature trough

to the east (marked with B, C, D, E) has developed into two cyclones, with an elongated streamer stretching between them. The mature cyclone (B) and developing cyclone (C), fed by the potential vorticity of the polar air, have wrapped moist subtropical air over the polar air (D, E), covering the dry air in the trough (F) and simultaneously increasing the interleaving of air masses that comprise the tropopause fold. The southernmost extent of the intrusion (G) is marked by weaker gradients and broken-up modeled folds caused by the gradual dispersion of a streamer that broke off anticyclonically from the trough about three days earlier. Likewise, the short, broken-up area to the far north (H) occurs because of a slow dispersion of moist, subtropical air at the subpolar latitudes that leads to slowly weakening gradients between air mass boundaries. It follows that the stratospheric intrusions at this boundary should break up and slowly disperse as well, as is indicated in the image. The curvature of two other features in the early trough (I, J) is caused by weaker developing cyclones.

## 7. Discussion

### 7.1. What the TFP Model Is, and What It Is Not

[27] The TFP model is designed to estimate the synoptic-scale distribution of tropopause folds in an extratropical domain defined by GOES-derived AWV imagery. When applied to individual events, the model is intended to act as a “first guess” estimate of tropopause fold distribution. For example, if this model were viewed as a tool for planning an airborne measurement campaign in the upper troposphere, then it is expected that this model would accurately predict where and when the tropopause folds are encountered, and that the predicted size of the folds would be imprecise individually but unbiased on average.

[28] It is important to note that the TFP model is not exactly a proxy for stratosphere-to-troposphere exchange. As a predictor for signs of tropopause folding associated with major upper tropospheric water vapor gradients, the model results include residual effects of tropopause folding as well as active cross-tropopause flux. *Bithell et al.* [2000] report residual structures of stratosphere-to-troposphere transport that remain coherent for as long as ten days after the period of development. Thus one can assume that much of the distribution of tropopause fold presence in reality is residual rather than actively developing. This largely explains the very significant difference between the amount of tropopause folding implied in this model (covering roughly half the area of the extratropical upper troposphere based on inspection of Figure 4e) and that implied by the ECMWF-based models of *Elbern et al.* [1998] and *Sprenger et al.* [2003] (each around 4% in the extratropical upper troposphere based on inspection of figures) which examined only actively developing folds resolved by a

**Figure 4.** (a) Cloud-truncated AWV image (units: altered brightness temperature, K) from 1200 UTC 30 April 2000. The AWV image uses the GOES-10 (west) water vapor channel. (b) Cloud-truncated AWV image from Figure 4a after smoothing ( $\sigma = 0.30$  g.c.d.). (c) Remotely sensed gradient (RSG) of Figure 4b, units are K g.c.d.<sup>-1</sup>. (d) Same as Figure 4c but with “ridge lines” marking boundaries with high spatial gradients, which indicate the openings of tropopause folds. (e) Smoothed AWV image (color bar units of degrees K), with ridge lines as in Figure 4d, and with estimated regions of tropopause folding (gray) reaching out from the ridge lines into the moist air mass, using a folding width of 2.11 great circle degrees (235 km); labels explained in text.

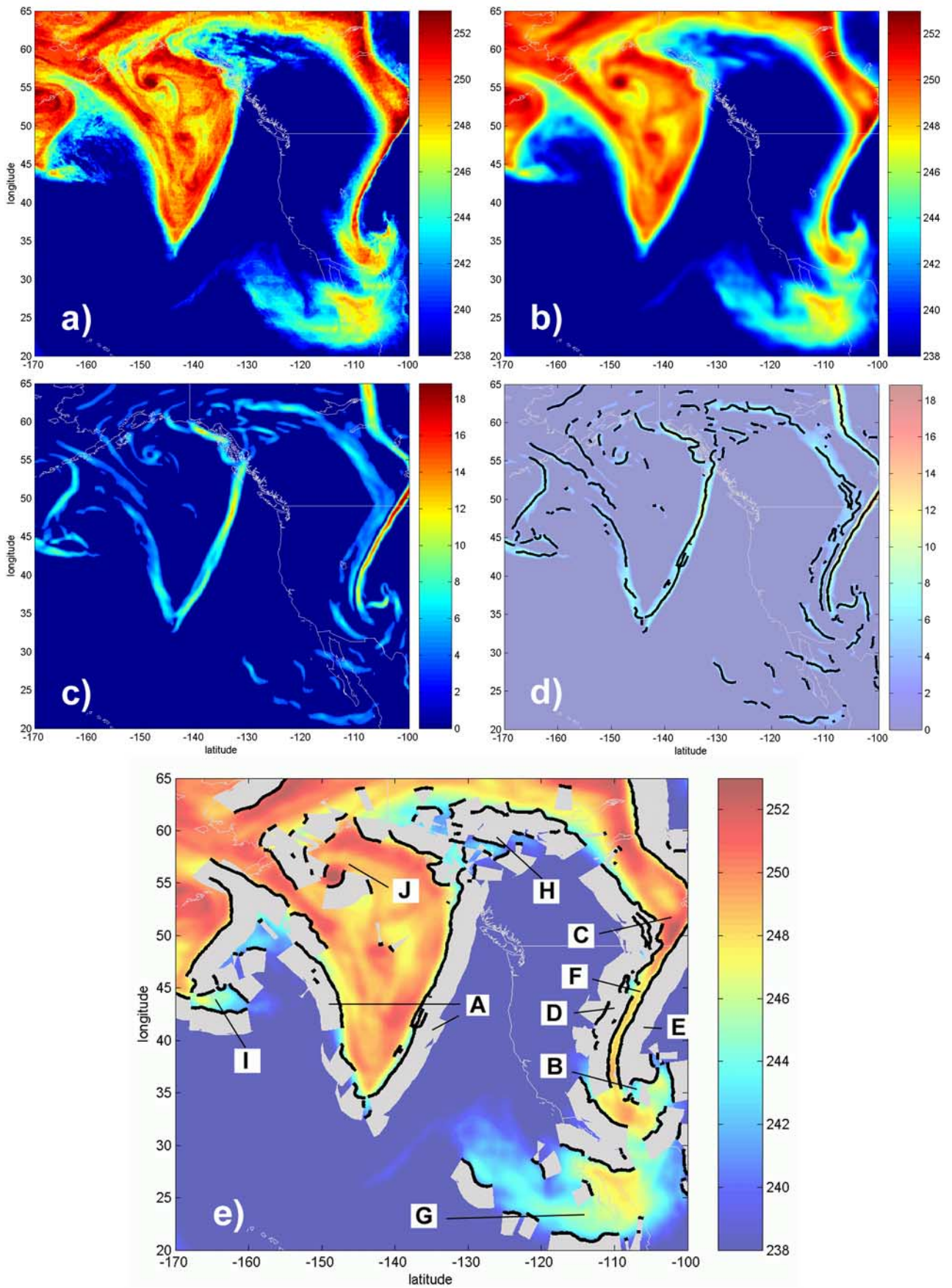


Figure 4

global reanalysis. Likewise, the differences of this model with the statistics of midlatitude tropopause folding from *Beekman et al.* [1997] derived from in situ soundings (a tropopause fold frequency of  $\sim 1\%$  from the University of Cologne algorithm and  $\sim 4\%$  from the “KMI/CNRS” algorithm) are due to their additional criteria that only counted layers of stratospherically enhanced air in the vicinity of the jet stream.

[29] Although it may seem counterproductive that the TFP model presents actively developing tropopause folds in the same way as residual ones, there is an inherent evenhandedness to this method of representation. The cross-tropopause mixing that occurs in conjunction with an actively developing tropopause fold is fairly obvious, but the slow, irreversible dispersion of large residual layers of stratospheric-type air is also a significant mechanism of cross-tropopause transport. This is recognized most naturally in the observation of cross-tropopause mixing through streamer breakdown [*Appenzeller et al.*, 1996]. This later stage of breakdown is less likely to be captured authentically in atmospheric models or reanalyses that rely on artificial diffusion to simulate sub-grid cell mixing. This does not necessarily limit the accuracy of a model or reanalysis to quantify cross-tropopause transport, but it does force these methods to focus on mixing at the scale of the model resolution. By contrast, the TFP model treats mixing across the tropopause as a continuous process from the inception of a tropopause fold to its breakdown into scales on the order of  $\sim 30$  km (the smoothed AWP product resolution) but it is continuously fixed to the real atmospheric system. In doing so, this model offers a unified conception of various mechanisms previously shown to lead to cross-tropopause flux. Whether in association with a midlatitude cyclone [*Danielsen*, 1968], an upper level geopotential trough [*Johnson and Vizee*, 1981], a cutoff low [*Vaughan and Price*, 1991] or a streamer [*Appenzeller et al.*, 1996] the actual location of mixing between chemically distinct air masses is at their outer boundaries, which extend horizontally into overlapping layers. Major boundaries are apparent in AWP imagery for each of these systems, indicating where the specific cross-tropopause mixing occurs throughout their evolution.

## 7.2. Limitations in the Design of the Model

### 7.2.1. Uniform Width

[30] The most obvious limitation of the model is its oversimplification of tropopause fold width as a uniform value, established from a limited number of observations. The accuracy of this approach in individual synoptic events has already been discussed. However, the frequency of tropopause folding averaged over the model’s entire domain is a separate issue. On the one hand, the average frequency of tropopause folding obtained by this model could be an underestimate, because in the parameterization, folding structures that were not measured end-to-end were thrown out of the calculation, which essentially excluded some folding structures for being too long (or in the terminology of this paper, “too wide”). On the other hand, the frequency could be overestimated due to the amount of double counting that takes place along gradient boundaries. In the parameterization, one boundary (flight 38) had two gradient magnitude peaks for one tropopause fold. In the TFP model, this

boundary would be assigned two tropopause folds for each gradient magnitude ridgeline. However, the effect of double counting on the overall modeled frequency of tropopause folding has been balanced in the most equitable way that the data allows by calculating the average fold width assuming a sample size of  $N + 1$  rather than  $N$  (from Table 1). Again, more data is needed to improve the accuracy and reduce the uncertainty of the model in this regard.

### 7.2.2. Short Folds

[31] The effect of “short folds” in the model is a possible issue as well. “Short folds” are the frequently occurring modeled folds whose length is considerably shorter than the standard fold width. These appear inherently unnatural because they indicate abrupt absences and reappearances of layering in the direction of the flow. They occur where an air mass boundary is skirting close to the gradient threshold, usually in the stage of growth or decay. When the boundary is barely under the threshold in some places and barely over in other places, the boundary is dashed with these short folds. This is a reasonable approximation for the real transitions that they represent, which are either the gradual appearance or disappearance of a fold. This phenomenon is exemplified well in the northern boundary of the subtropical air mass in Figure 4e indicated by “H.” The reason that this is a concern for the accuracy in the model is that “short folds” were never encountered in the model parameterization data set. Therefore, if these features are actually not as long as the model depicts, then they exaggerate the tropopause fold frequency in places where they occur most heavily. Observation of the whole set of model results reveals that “short folds” contributed to the tropopause fold distributions more with latitude.

[32] Although “short folds” are probably not as common in reality as in the model, and one may argue the case that they bias the results, an even stronger case can be made that short folds are a fair approximation for tropopause folding in areas in which the activity is weaker.

### 7.2.3. Ridgeline Curvature

[33] In the TFP model, the boundaries assigned to the openings of tropopause folds sometimes have a curvature that may be unrealistic, because the lines contour along small undulations in the gradient field below the scale of the smoothing parameter. If this aspect of the model is a source of error, it is too difficult to detect with the data on hand. A solution would have to come from more advanced treatment of these boundaries that adds a small amount of “tension” to the ridge lines to reduce the curvature [*Kass et al.*, 1987].

### 7.2.4. TFP and Cross-Tropopause Flux

[34] The model is not equipped to answer directly a number of issues concerning the mass flux between the stratosphere and troposphere. The model does not lead directly to any quantitative estimate of the mass flux associated with the modeled tropopause fold structures. Such an estimate would require an extra parameter describing the “efficiency” with which the mass of air inside the folding structure mixes with its surrounding environment, and this is outside the scope of this study. This estimate would be complicated significantly by the degree to which folded structures are influenced by the recirculation of air between the troposphere and stratosphere. Another complicating factor is the significant number of cyclones that are re-constituted from previous cyclonic systems and whose

upper tropospheric and lower stratospheric air are less chemically distinct than normal.

### 7.2.5. Limited Domain of the Samples

[35] *Wimmers and Moody* [2004] addressed the issues related to the limited domain of the sample folds. These issues are summarized as follows: (1) The samples were limited to the February–May time period, in which baroclinicity and downward forcing are higher; (2) All samples were roughly within the midlatitudes (40–65°N); (3) All samples were over land and not ocean, where AWV gradients appear stronger; and (4) Not many samples are provided for each category of synoptic boundary, such as polar/subtropical air mass boundary or streamer edge. Undoubtedly, more transects of airborne lidar are needed to make this model more robust. However, issues 3 and 4 only speculate the possibility of a difference between these domains, and it is likely that the land/sea difference and boundary difference only affect the gradient magnitudes, not the relationship between gradient magnitude and tropopause folding. On the other hand, issues 1 and 2 are more likely to result in real differences in the relationship between gradient magnitude and tropopause folding, so it follows that the best application of this model is between the months of February and May and within the spatial domain of the midlatitudes.

### 7.3. Applications

[36] There are two applications that suit this model best. The first is to use the TFP model as a “nowcasting” tool in an aircraft measurement campaign to design the most advantageous flight path in real time that avoids tropopause folds, maximizes their sampling, or draws a fair and representative sample of their presence in a region of interest. The second application is to develop a climatology of tropopause fold presence that is based uniquely on fine-resolution geostationary satellite observations associated with tropopause folding activity. This would address the relative distribution of stratospheric-type layers of air at tropospheric levels, which is complementary to the results of other studies that estimate the global distribution of cross-tropopause flux based on global analysis wind fields [e.g., *James et al.*, 2003; *Sprenger and Wernli*, 2003]. A satellite-based climatology developed over the domain of the TOPSE project (North America, February to May 2000) is explored in a subsequent paper.

## 8. Summary and Conclusions

[37] The main points of this study are as follows:

[38] 1. The hypotheses that the “folded mass” of ozone in a tropopause fold or the “fold width” is proportional to the AWV remotely sensed gradient is not supported by the data.

[39] 2. Assuming that a remotely sensed gradient above the established threshold is indicative of active mass flux from the stratosphere, the lack of a proportional relationship between the AWV remotely sensed gradient and folded mass shows that tropopause folds do not commonly reach a “steady state” mass of ozone inside the fold. Rather, the mass of air must be controlled at least as much by a combination of the age of the fold and dynamical dispersion mechanisms not connected to the strength of the tropopause depression. This has important implications for the interpretation of upper tropospheric lidar and in situ ozone data at tropopause folds in the midlatitudes.

[40] 3. The average folded mass corresponding to a ridgeline in the  $|\nabla_{ABT}'''|$  image is  $30.4 \text{ kg m}^{-1}$ . The average fold width is 2.11 great circle degrees (235 km).

[41] 4. A model predicting the presence of tropopause folding (the TFP model) is achieved by an image processing of the AWV product that involves a) cloud masking, b) image smoothing, c) gradient magnitude calculation, d) resolving “ridge lines” and e) assigning a constant width tropopause fold at the boundary and pointing toward the moister air mass.

[42] 5. The modeled distribution of tropopause folds is entirely consistent with the finding of *Johnson and Vezze* [1981] that tropopause folds are associated along the flanks of nearly every geopotential trough.

[43] 6. The TFP model estimates the distribution of both active and residual tropopause folds, which is a useful method of tracking the dispersion of stratospherically enhanced air into the troposphere and is unique to this observation-based model of tropopause folding.

[44] The principal strength of this model is in estimating the presence of tropopause folding based on real observations. The methods of this model are not yet perfected, nor is it parameterized from a large enough set of data. Many improvements can still be made using more advanced image processing techniques, ancillary models and data, or improved remote sensing instruments. This paper is seen as a first step in a promising approach to exploiting satellite data quantitatively in the process of analyzing tropopause folding in order to complement the currently existing methods of modeling, in situ observation and lidar observation.

## Appendix A: Approximating Perpendicular Transects With the Data

### A1. Estimating the Width and Area of the Tropopause Fold Cross Section

[45] Although the boundaries of a fold are easy to identify by observation in the lidar image, there is no known way to calculate their positions objectively. The main reason for this is that a tropopause fold by its very nature is a place in which two regions of air blend together, so the locations that signify its outer limits are not easily defined. To substitute for an objective method, the locations of the fold opening and tail were determined through a subjective estimation of the fold area. In this method, the fold area is approximated as a trapezoid with parallel vertical sides at the opening and tail. The position of the opening is identified as the location at which the most closely packed contours separating stratospheric levels of ozone from tropospheric levels are oriented vertically. The position of the tail is the location beyond which the ozone contours show little or no connection with the stratospheric intrusion of ozone. Similarly, the upper and lower bounds of the folds are straight lines imposed on the image that approximate the boundary between high stratospheric-type concentrations of ozone and background tropospheric concentrations.

[46] The width of the fold as observed by the lidar is simply

$$W_{lidar} = \| \mathbf{p}_{opening} - \mathbf{p}_{tail} \|, \quad (\text{A1})$$

where  $\| \cdot \|$  is the vector length operator and  $\mathbf{p}_{opening}$  and  $\mathbf{p}_{tail}$  are the geographic positions of the opening and tail of

the fold in the lidar, respectively. This width term equates to the width of the fold in a perpendicular cross section only if the angle of incidence ( $\alpha$ ) is  $0^\circ$ . Otherwise, the calculation for the cross-sectional width, used in this study, is

$$W_{\text{tf}} \cong W_{\text{lidar}} \cdot \cos \alpha. \quad (\text{A2})$$

## A2. Computing the Mass of Ozone and Mass of Air per Unit Length in the Tropopause Fold

[47] Integrating mass of ozone from a straight lidar transect perpendicular to a fold would be a straightforward calculation, but the circumstances of the lidar measurements in TOPSE require additional treatment. Ideally, a straight, perpendicular lidar transect yields an integrated mass per unit length of

$$m_{O_3} = N_A M_{O_3} \int_{\text{opening}}^{\text{tail}} \int_{\text{bottom}}^{\text{top}} n_{O_3} dz dw, \quad (\text{A3})$$

where  $N_A$  is Avogadro's number;  $M_{O_3}$  is the molecular weight of ozone;  $z$  and  $w$  are the height and width coordinates, respectively; and  $n_{O_3}$  is the ozone number density. Although lidar retrievals are usually displayed in their transects as mixing ratio (ppbv), the original retrieval is measured as number density ( $n_{O_3}$ , molecules  $\text{cm}^{-3}$ ), which is a more direct pathway to calculating ozone mass. The translation of the above formula into discrete intervals is then

$$m_{O_3} \cong N_A M_{O_3} \sum_{\text{opening}}^{\text{tail}} \sum_{\text{bottom}}^{\text{top}} n_{O_3} \Delta z \Delta w, \quad (\text{A4})$$

but if  $\Delta z$  and  $\Delta w$  are first-order linear over the domain of the summation, then equation (A4) reduces to the following (using the formula for the area of a trapezoid)

$$m_{O_3} \cong N_A M_{O_3} \bar{n}_{O_3} W_{\text{tf}} [0.5 \cdot (h_{\text{opening}} + h_{\text{tail}})], \quad (\text{A5})$$

where  $h_{\text{opening}}$  and  $h_{\text{tail}}$  are the heights of the opening and tail of the fold, respectively. It is also an important point that a straight but nonperpendicular transect would yield the same value of ozone number density:

$$\bar{n}_{O_3} = (\bar{n}_{O_3})_{\text{lidar}}. \quad (\text{A6})$$

[48] The important issue behind this examination is whether the average ozone of the lidar transects are roughly equal to that of a perpendicular transect, and thus able to apply to equation (A6). This depends primarily on whether the lidar transect over-represents or under-represents certain locations of a heterogeneous tropopause fold that fall outside the mean ozone concentrations. However, an examination of the lidar transects shows that the folds selected in this study have been measured "fairly," that is, with equal emphasis on all segments of the folds horizontally. The one exception to this rule was the lidar transect on flight 42, which sampled a short segment in the middle of the fold for approximately 40 min during a spiral-down in the flight. However, since the middle of the fold contained values of ozone number density that were close to average for the

fold, then the average value for flight 42 is also a valid average. Thus, combining equations (A2), (A5), and (A6) and considering the discussion above, the actual lidar transects approximate the folded mass per unit length as

$$m_{O_3} \cong 0.5 \cdot N_A M_{O_3} (\bar{n}_{O_3})_{\text{lidar}} W_{\text{lidar}} (h_{\text{opening}} + h_{\text{tail}}) \cos \alpha. \quad (\text{A7})$$

[49] By the same argument, the total mass of air (per unit length) inside the trapezoid perimeter of the tropopause fold is theoretically

$$m_{\text{f}} = \int_{\text{opening}}^{\text{tail}} \int_{\text{bottom}}^{\text{top}} \rho dz dw, \quad (\text{A8})$$

where  $\rho$  is the density of air at locations within the fold. In this analysis, the mass of air within the perimeter of the fold is calculated with the same climate average of density that is used in the lidar retrievals to convert ozone number density to concentration [Jursa, 1985]. The climate average density is a function of latitude ( $\theta$ ), height ( $z$ ) and time of measurement (to the nearest month,  $mon$ ), so the average density of air in a lidar tropopause fold is

$$\bar{\rho}_{\text{lidar}} \cong N^{-1} \sum_{i \in \text{fold}} \rho(\theta_i, z_i, mon_i). \quad (\text{A9})$$

Since the conditions for extending lidar transects to perpendicular transects are no different in this case than in the previous case of ozone transects, then the approximation for the mass of the tropopause fold is carried out in the same manner as for equation (A7):

$$m_{\text{f}} \cong 0.5 \cdot \bar{\rho}_{\text{lidar}} W_{\text{lidar}} (h_{\text{opening}} + h_{\text{tail}}) \cos \alpha. \quad (\text{A10})$$

The dimensions of equation (A10) are mass of air per unit length.

## A3. Computing the Remotely Sensed Gradient

[50] Every fold transect in the lidar has a counterpart flight transect through a remotely sensed gradient in the AWV imagery. In this section, the term "gradient ridge" describes the individual features in  $(GM - \tau)$  as shown in Figure 4c. In reality, it is fair to approximate the remotely sensed gradient (equation (2)) as a mean of  $(GM - \tau)$  across the associated gradient ridge the width of the gradient ridge. This is because in this data set each flight path traveled in a nearly straight line across each gradient ridge, mostly due to the thin width of the ridges in comparison to the length of the flight track. The width of the gradient ridge transect is calculated as

$$W_{\text{grt}} = \| \mathbf{p}_{\text{start}} - \mathbf{p}_{\text{finish}} \|, \quad (\text{A11})$$

where  $\mathbf{p}_{\text{start}}$  and  $\mathbf{p}_{\text{finish}}$  are the beginning and end points of the transect through the gradient ridge, respectively. This relates to the width of a parallel transect through a ridge as the following:

$$W_{\perp \text{grt}} = W_{\text{grt}} \cos \beta, \quad (\text{A12})$$

where  $\beta$  is the angle of incidence between the flight track and the normal of the gradient ridge.

[51] Thus the remotely sensed gradient can be approximated with the real transect data as

$$RSG \cong \overline{(GM - \tau)} \cdot W_{grt} \cos \beta. \quad (A13)$$

[52] **Acknowledgments.** Support for this work was provided by NSF under the TOPSE project, grant OPP-9908840, by NOAA/NESDIS (award NA96ECO011), and by the Space Science and Engineering Center of the University of Wisconsin. We wish to thank the Ph.D. committee members Jose Fuentes, Steven Macko, and Scott Acton at the University of Virginia for their constructive input on the dissertation on which this work is based.

## References

- Appenzeller, C., H. C. Davies, and W. A. Norton (1996), Fragmentation of stratospheric intrusions, *J. Geophys. Res.*, *101*, 1435–1456.
- Beekman, M., et al. (1997), Regional and global tropopause fold occurrence and related ozone flux across the tropopause, *J. Atmos. Chem.*, *28*, 29–44.
- Bithell, M., G. Vaughan, and L. J. Gray (2000), Persistence of stratospheric ozone layers in the troposphere, *Atmos. Environ.*, *34*(16), 2563–2570.
- Chen, P. (1995), Isentropic cross-tropopause mass-exchange in the extratropics, *J. Geophys. Res.*, *100*, 16,661–16,673.
- Cristofanelli, P., et al. (2003), Stratosphere-to-troposphere transport: A model and method evaluation, *J. Geophys. Res.*, *108*(D12), 8525, doi:10.1029/2002JD002600.
- Danielsen, E. F. (1968), Stratospheric-tropospheric exchange based on radioactivity, ozone and potential vorticity, *J. Atmos. Sci.*, *25*, 502–518.
- Elbern, H., J. Hendricks, and A. Ebel (1998), A climatology of tropopause folds by global analyses, *Theor. Appl. Climatol.*, *59*(3–4), 181–200.
- Gettelman, A., and A. H. Sobel (2000), Direct diagnosis of stratosphere-troposphere exchange, *J. Atmos. Sci.*, *57*, 3–16.
- Goering, M. A., W. A. Gallus, M. A. Olsen, and J. L. Stanford (2001), Role of stratospheric air in a severe weather event: Analysis of potential vorticity and total ozone, *J. Geophys. Res.*, *106*, 1813–1823.
- James, P., A. Stohl, C. Forster, S. Eckhardt, P. Seibert, and A. Frank (2003), A 15-year climatology of stratosphere-troposphere exchange with a Lagrangian particle dispersion model: 1. Methodology and validation, *J. Geophys. Res.*, *108*(D12), 8519, doi:10.1029/2002JD002637.
- Johnson, W. B., and W. Viezee (1981), Stratospheric ozone in the lower troposphere—I. Presentation and instrumentation of aircraft measurements, *Atmos. Environ.*, *15*(7), 1309–1323.
- Jursa, A. S. (1985), *Handbook of Geophysics and the Space Environment*, Air Force Geophys. Lab., Hanscom AFB, Mass.
- Kass, M., A. Witkin, and D. Terzopoulos (1987), Snakes: Active contour models, *Int. J. Comput. Vision*, *1*, 321–331.
- Kowol-Santen, J., H. Elbern, and A. Ebel (2000), Estimation of cross-tropopause air mass fluxes at midlatitudes: Comparison of different numerical methods and meteorological situations, *Mon. Weather Rev.*, *128*, 4045–4057.
- Lamarque, J. F., and P. G. Hess (1994), Cross-tropopause mass-exchange and potential vorticity budget in a simulated tropopause folding, *J. Atmos. Sci.*, *51*(15), 2246–2269.
- Meloan, J., P. C. Siegmund, and M. Sigmond (2001), A Lagrangian computation of stratosphere-troposphere exchange in a tropopause-folding event in the subtropical Southern Hemisphere, *Tellus, Ser. A*, *53*, 368–379.
- Meloan, J., et al. (2003), Stratosphere-troposphere exchange: A model and method intercomparison, *J. Geophys. Res.*, *108*(D12), 8526, doi:10.1029/2002JD002274.
- Newell, R. E., V. Thouret, J. Y. N. Cho, P. Stoller, A. Marengo, and H. G. Smit (1999), Ubiquity of quasi-horizontal layers in the troposphere, *Nature*, *398*, 316–319.
- Olsen, M. A., W. A. Gallus Jr., J. L. Stanford, and J. M. Brown (2000), Fine-scale comparison of TOMS total ozone data with model analysis of an intense midwestern cyclone, *J. Geophys. Res.*, *105*, 20,487–20,495.
- Ravetta, F., G. Ancellet, J. Kowol-Santen, R. Wilson, and D. Nedeljkovic (1999), Ozone, temperature, and wind field measurements in a tropopause fold: Comparison with a mesoscale model simulation, *Mon. Weather Rev.*, *127*, 2641–2653.
- Seo, K.-H., and K. P. Bowman (2001), A climatology of isentropic cross-tropopause exchange, *J. Geophys. Res.*, *106*(D22), 28,159–28,172.
- Seo, K.-H., and K. P. Bowman (2002), Lagrangian estimate of global stratosphere-troposphere mass exchange, *J. Geophys. Res.*, *107*(D21), 4555, doi:10.1029/2002JD002441.
- Sprenger, M., and H. Wernli (2003), A Northern Hemispheric climatology of cross-tropopause exchange for the ERA15 time period (1979–1993), *J. Geophys. Res.*, *108*(D12), 8521, doi:10.1029/2002JD002636.
- Sprenger, M., M. Croci Maspoli, and H. Wernli (2003), Tropopause folds and cross-tropopause transport: A global investigation based upon ECMWF analyses for the time period March 2000 to February 2001, *J. Geophys. Res.*, *108*(D12), 8518, doi:10.1029/2002JD002587.
- Stohl, A. (2001), A 1-year Lagrangian “climatology” of airstreams in the Northern Hemisphere troposphere and lowermost stratosphere, *J. Geophys. Res.*, *106*(D7), 7263–7279.
- Stohl, A., and D. J. Thomson (1999), A density correction for Lagrangian particle dispersion models, *Boundary Layer Meteorol.*, *90*, 155–167.
- Stohl, A., M. Hittenberger, and G. Wotawa (1998), Validation of the Lagrangian particle dispersion model FLEXPART against large scale tracer experiments, *Atmos. Environ.*, *32*, 4245–4264.
- Stohl, A., et al. (2003), Stratosphere-troposphere exchange: A review, and what we have learned from STACCATO, *J. Geophys. Res.*, *108*(D12), 8516, doi:10.1029/2002JD002490.
- Vaughan, G., and J. D. Price (1991), On the relation between total ozone and meteorology, *Q. J. R. Meteorol. Soc.*, *117*, 1281–1298.
- Vaughan, G., H. Gouget, F. M. O’Connor, and D. Wier (2001), Fine-scale layering on the edge of a stratospheric intrusion, *Atmos. Environ.*, *35*, 2215–2231.
- Wei, M.-Y. (1987), A new formulation of the exchange of mass and trace constituents between the stratosphere and troposphere, *J. Atmos. Sci.*, *44*, 3079–3086.
- Wernli, H., and M. Bourqui (2002), A Lagrangian “1-year climatology” of (deep) cross-tropopause exchange in the extratropical Northern Hemisphere, *J. Geophys. Res.*, *107*(D2), 4021, doi:10.1029/2001JD000812.
- Wimmers, A. J. (2003), Satellite-based location of tropopause folding signatures along air mass boundaries, Ph.D. dissertation, Univ. of Va., Charlottesville, Va.
- Wimmers, A. J., and J. L. Moody (2001), A fixed-layer estimation of upper tropospheric specific humidity from the GOES water vapor channel: Parameterization and validation of the altered brightness temperature product, *J. Geophys. Res.*, *106*, 17,115–17,132.
- Wimmers, A. J., and J. L. Moody (2004), Tropopause folding at satellite-observed spatial gradients: 1. Verification of an empirical relationship, *J. Geophys. Res.*, D19306, doi:10.1029/2003JD004145.
- Wirth, V. (1995), Comments on “A new formulation of the exchange of mass and trace constituents between the stratosphere and troposphere,” *J. Atmos. Sci.*, *52*, 2491–2493.
- Wirth, V., and J. Egger (1999), Diagnosing extratropical synoptic-scale stratosphere-troposphere exchange: A case study, *Q. J. R. Meteorol. Soc.*, *126*, 635–656.
- Wirth, V., C. Appenzeller, and M. Juckes (1997), Signatures of induced vertical air motion accompanying quasi-horizontal roll-up of stratospheric intrusions, *Mon. Weather Rev.*, *125*, 2504–2519.

J. L. Moody, Department of Environmental Sciences, University of Virginia, Charlottesville, VA 22093, USA.

A. J. Wimmers, CIMSS, University of Wisconsin-Madison, 1225 W. Dayton St., Madison, WI 53706, USA. (wimmers@ssec.wisc.edu)